

Protected ultrathin cuprous oxide film for photocatalysis: Excitation and relaxation dynamics

Jan Beckord¹, J. Trey Diulus^{1,2}, Zbynek Novotny^{1,2,*}, Jürg Osterwalder¹ and Matthias Hengsberger^{1,†}¹Department of Physics, University of Zurich, Winterthurerstrasse 190, 8057 Zurich, Switzerland²Swiss Light Source, Paul Scherrer Institute, Forschungsstrasse 111, 5232 Villigen, Switzerland

(Received 15 December 2022; accepted 22 March 2023; published 6 April 2023)

In the search for cost-effective ways to produce green hydrogen, harnessing the most abundant renewable energy source—sunlight—directly through photoelectrochemical water splitting is highly desirable. Cuprous oxide (Cu_2O) has proven itself as a material with great potential for the hydrogen evolution reaction (HER) and stands out by its Earth abundance and low processing cost. In this photoelectron spectroscopy study we investigated the electron dynamics in a heterostructure comprised of a Cu_2O surface oxide grown on $\text{Cu}(111)$ underneath a hexagonal boron nitride ($h\text{-BN}$) film, which replaces a conventional capping layer for corrosion protection. Our results show that it can be a viable cuprous oxide-based photoelectrode material. The $h\text{-BN}$ film stays intact during the oxidation, and the oxide layer forms an ordered structure with defined valence and conduction bands. The conduction band is at a suitable energy to drive the HER for water splitting, but the photoexcited electrons display short lifetimes. Electrons are mainly excited in the copper substrate and are then captured in long-lived defect states in the Cu_2O layer. The water splitting efficiency of this photocathode may still be improved by reducing the defect density.

DOI: [10.1103/PhysRevMaterials.7.045801](https://doi.org/10.1103/PhysRevMaterials.7.045801)

I. INTRODUCTION

In the growing efforts to mitigate the impact of climate change, the reduction of greenhouse gas emissions is a central objective. Photoelectrochemical water splitting offers a realistic pathway towards a sustainable energy grid that is powered by climate-neutral fuels. The water splitting reaction consists of the hydrogen evolution reaction (HER) and the oxygen evolution reaction (OER) simultaneously occurring on two separate photoelectrodes, which are driven by photoexcited electrons and holes, respectively. The biggest challenge is designing a simple and reliable cell out of cheap materials that can be prepared with relative ease. Cuprous oxide (Cu_2O) is one of the most promising photocathode materials due to being an earth-abundant semiconductor with the desired photocatalytic properties [1]. Many working designs have been demonstrated by band gap engineering with protective capping layers [1,2] and complementing photoanodes [3]. Some designs are produced in an industrially scalable way by oxidizing flexible copper substrates without extra processing steps [4], but these cathodes suffer from corrosion in the aqueous environment and are only functional for a short time.

Moreover, recent device measurements and simulations [5] have highlighted that surface or interface defects are highly detrimental to the efficiency and special precautions must be taken during the deposition of overlayers to prevent defect formation. Time-resolved two-photon photoemission studies [6,7] have investigated the reasons for the low efficiency, finding that defect states at the surface capture conduction band electrons before they can drive a water splitting reaction. To avoid modifying the freshly prepared Cu_2O surface we have devised a simple design that grows it as the last step. We achieve this by oxygen intercalation underneath a monolayer of hexagonal boron nitride ($h\text{-BN}$) deposited on $\text{Cu}(111)$.

The large-scale epitaxial growth of highest quality $h\text{-BN}$ on $\text{Cu}(111)$ wafers [8,9] and copper foils [10,11] has already been extensively studied and perfected, making it an ideal starting point for more advanced heterostructures [12]. This atomically thin capping layer significantly increases the corrosion resistance in aqueous environments [13] and has exceptional catalytic properties [14]. The catalytic transparency of $h\text{-BN}$ has been demonstrated for different reactions like the oxygen reduction reaction in hydrogen fuel cells [15], graphene growth [16,17], and CO oxidation [18]. DFT calculations regarding these results suggest that electrons can migrate through the $h\text{-BN}$ layer while the substrate is chemically protected. Nevertheless, we were able to intercalate oxygen at the $h\text{-BN}$ domain boundaries. Our surface characterization after the oxidation shows that we obtain a highly ordered Cu_2O -like monolayer without destroying the $h\text{-BN}$ [19]. Previous studies of the oxidation protection of $h\text{-BN}$ and graphene monolayers on metals show that it is highly dependent on the quality of the $h\text{-BN}$ monolayer, the oxygen pressure, and the sample temperature [20–22]. Scardamaglia *et al.* [22] did not observe any intercalated

*Present address: Laboratory for Joining Technologies and Corrosion, Empa, Swiss Federal Laboratories for Materials Science and Technology, Ueberlandstrasse 129, 8600 Dübendorf, Switzerland.

†Corresponding author: matthias.hengsberger@physik.uzh.ch

Published by the American Physical Society under the terms of the Creative Commons Attribution 4.0 International license. Further distribution of this work must maintain attribution to the author(s) and the published article's title, journal citation, and DOI.

Cu_2O underneath h -BN with ambient pressure x-ray photoelectron spectroscopy (AP-XPS) below 300 °C. In contrast, using Raman spectroscopy, Galbiati *et al.* [21] detected a small amount of Cu_2O underneath the h -BN layer for temperatures between 150 °C and 300 °C, which agrees with our results. A study on Ru(0001) corroborates the interpretation of oxygen intercalation at grain boundaries [23]. The ability to intercalate gas molecules into the confined space underneath the two-dimensional (2D) material opens up rich possibilities of confined catalysis [12,14,24].

In this paper we will focus on the photocatalytic water splitting aspect, but future experiments with our heterostructure may reveal additional use cases. First, we outline the experimental setup and our sample preparation methods following the recipe described in [19]. We characterize the sample with x-ray photoelectron spectroscopy (XPS) and low-energy electron diffraction (LEED), revealing the ordered Cu_2O -like surface oxide and the intact h -BN layer. We then show the valence and conduction band structure with UV photoelectron spectroscopy (UPS) and two-photon photoelectron spectroscopy (2PPE) and compare the electronic states to unoxidized h -BN/Cu(111) and bulk Cu_2O (111). We identify the valence and conduction bands of the Cu_2O -like surface oxide, which are both lower in energy than on bulk Cu_2O , and observe the expected band structure of h -BN. Time-resolved 2PPE reveals a short relaxation time of the conduction band and a strong defect state at the Fermi level that is populated by hot electron capture from the metallic substrate. We conclude with the proposed energy and excitation scheme of this heterostructure and its implications for photocatalytic water splitting.

II. EXPERIMENTAL METHODS

A. Experimental setup

The sample was prepared in an ultrahigh vacuum preparation chamber with a base pressure $<10^{-9}$ mbar and transferred to the analysis chamber with a base pressure of 2×10^{-10} mbar for *in situ* photoelectron spectroscopy. The analysis chamber is a modified Vacuum Generators ESCALAB 220 design [25] with a dual anode x-ray source providing Mg K_α and Si K_α photons with energies of $h\nu = 1253.6$ eV and $h\nu = 1740.0$ eV, respectively. The He I α photons with $h\nu = 21.22$ eV for Fig. 1 are generated by a Gammatdata VUV 5050 microwave driven monochromated He plasma source. All measurements were performed at room temperature.

After the characterization, the sample was transferred in a vacuum suitcase to the time-resolved photoemission chamber described in [26]. This chamber is equipped with a SPECS PHOIBOS 150 WAL hemispherical electron analyzer with a 2D detector and a wide-angle lens with 60° acceptance angle for fast acquisition of angle-resolved photoemission spectra (ARPES). A nonmonochromated helium lamp is used for He II α ARPES in Fig. 2, emitting the main He II α line at $h\nu = 40.81$ eV and a noticeable He II β satellite at $h\nu = 48.37$ eV. The base pressure of this chamber is below 2×10^{-10} mbar.

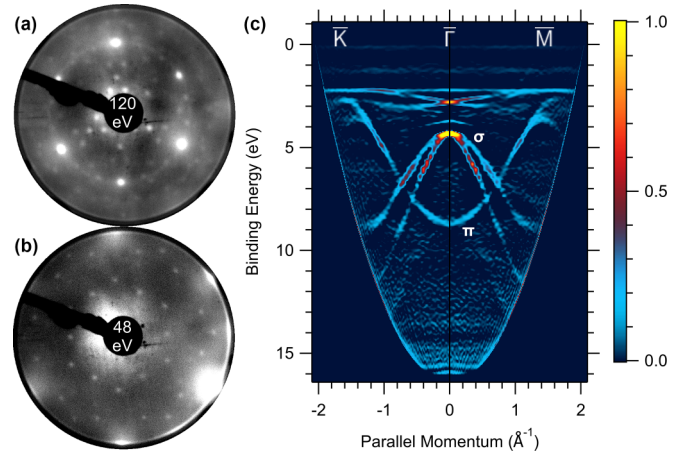


FIG. 1. LEED images at (a) 120 eV and (b) 48 eV after the first preparation. (c) h -BN/ Cu_2O /Cu(111) ARPES, combined from angular scans in the \bar{K} and \bar{M} directions.

Femtosecond laser pulses for time-resolved 2PPE are generated in a mode-locked Coherent Mira Ti:sapphire oscillator with a Coherent RegA 9050 regenerative chirped pulse amplifier at a repetition rate of 100 kHz. The pulses have a wavelength of 820 nm with a spectral width of 36 nm and a pulse energy of 6 μJ . The pulses are frequency-doubled in a β -barium borate (BBO) crystal and then split in a beam splitter. One beam serves as the pump pulse and is routed over a computer-controlled delay stage. The other beam is frequency-doubled again in a second BBO crystal and then dispersion-compensated with a CaF_2 prism compressor. The pump beam is not dispersion compensated. Both beams are made p -polarized with respect to the sample by $\lambda/2$ wave plates, and the pulse energies are adjusted with neutral density filters. Finally, the beams are recombined and focused collinearly onto the sample. The measured wavelengths and Gaussian widths are $\lambda_{\text{Pump}} = 413 \pm 4$ nm, $h\nu_{\text{Pump}} = 3.00 \pm 0.03$ eV and $\lambda_{\text{Probe}} = 208 \pm 1$ nm, $h\nu_{\text{Probe}} = 5.96 \pm 0.03$ eV. The beam profile was measured with a CMOS camera and fitted with a 2D Gaussian, giving a $1/e^2$ beam waist of 85 μm for the pump pulse and 65 μm for the probe pulse as shown in Fig. S8 of the Supplemental Material [27]. For the time-resolved spectra, a bias voltage of -5 V was applied to the sample and the Fermi level was determined from the spectra at negative delays. The not-time-dependent background at negative delays was then subtracted.

B. Sample preparation

The Cu(111) single crystal with 7 mm diameter was sputtered with Ar^+ ions at 1.5 keV acceleration voltage and 0.5 μA sample current for 20 min, and then annealed at 1050 K for 20 min. A second sputter/anneal cycle was done with 10 min duration each. The sample cleanliness and surface order were monitored by x-ray photoelectron spectroscopy (XPS) and low-energy electron diffraction (LEED), respectively. We found little carbon contamination of 0.11 ± 0.02 atoms per surface unit cell that could not be further reduced by more cleaning cycles or by the subsequent oxidation. After

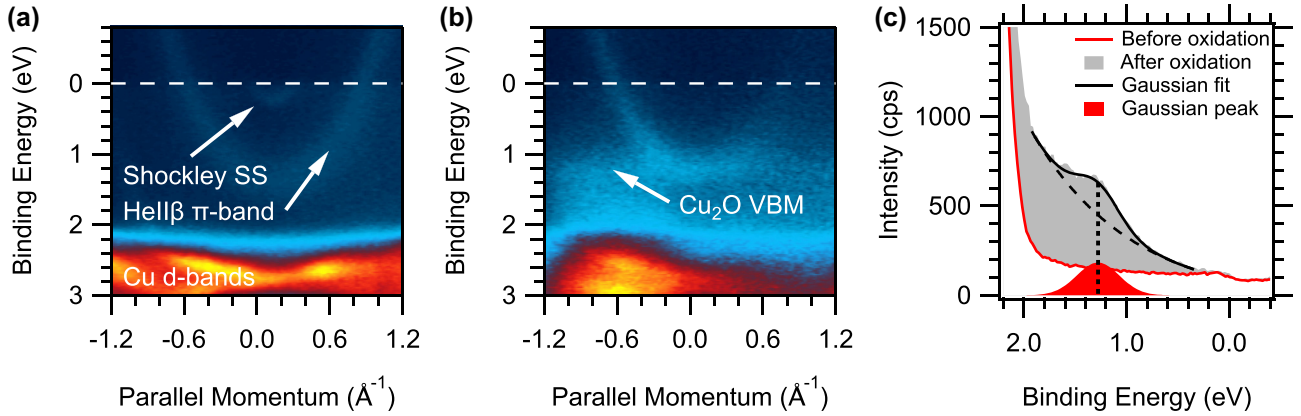


FIG. 2. (a) Detail from a He II α spectrum of h -BN/Cu(111) including the Fermi edge, the Shockley surface state, the He II β satellite of the h -BN π -band, and the onset of the Cu d bands. (b) Same region after oxidation with logarithmic color scale for both images. The surface state vanishes and an additional band above the d bands appears. (c) Gaussian fit with exponential background of the spectrum after oxidation integrated between -0.7 and -1.2 \AA^{-1} , with the spectrum before oxidation for reference. The Gaussian peak assigned to the Cu₂O valence band is centered at $E_B = 1.28 \pm 0.01 \text{ eV}$ with the FWHM $0.48 \pm 0.01 \text{ eV}$.

the second anneal cycle, hexagonal boron nitride was grown by chemical vapor deposition (CVD) of borazine ($\text{B}_3\text{N}_3\text{H}_6$) at 4×10^{-6} mbar for 11 min for a dose of 2000 Langmuir with the sample temperature held at 1050 K.

The oxide thin film of the first preparation was grown by oxygen intercalation at 0.08 mbar O_2 pressure for 5 min with the sample at 430 K. In the second preparation, the oxygen pressure was held at 0.10 mbar for 10 min instead. The oxygen exposures are 1.8×10^7 and $4.5 \times 10^7 \text{ L}$, respectively. These high exposures are necessary to overcome the protective h -BN layer, but the h -BN layer is not affected despite the high oxygen exposures [19].

III. RESULTS

A. Physical characteristics

The surface was characterized with XPS and LEED to compare with the preparation described in [19]. A more thorough investigation of the surface structure is given therein. The XPS results in Fig. S1 [27] show that the h -BN layer is still intact after the oxide preparation with a B : N stoichiometry $(1.03 \pm 0.03) : 1$, but the N $1s$ and B $1s$ peaks are shifted by 0.3 eV to lower binding energies relative to the Fermi level, showing an increased work function. The reason for the shift is that the h -BN layer is weakly bound and far away from the surface, so its electronic states are aligned to the shifted vacuum level instead of the Fermi level [28]. The O $1s$ peak indicates a Cu₂O-like overlayer with an oxygen coverage of 0.6 ± 0.1 atoms per primitive surface unit cell, indicating a thickness of one monolayer. The longer oxidation in the second preparation does not lead to a thicker oxide layer, but a reduced defect density, as will be shown later.

A LEED image at 120 eV kinetic energy [Fig. 1(a)] contains the six principal spots of the Cu(111) surface unit cell, a faintly visible ring from the different rotational domains of h -BN, and many spots from the oxide layer. This pattern agrees with the one observed by Judd *et al.* [29], which they

assign to a $|\begin{smallmatrix} 3 & 2 \\ -1 & 2 \end{smallmatrix}|$ overlayer with three rotational domains. Different spots from the same pattern are visible at 48 eV [Fig. 1(b)]. LEED images before oxidation and at other energies are provided in Figs. S2–S4 [27] with further discussion of the structure. These results confirm that our method reproducibly forms a well-ordered surface oxide below the h -BN layer by intercalation without destroying it.

B. Electronic valence band structure

The He I α ARPES spectra after oxidation [Fig. 1(c)] clearly show the sharp σ and π bands of an intact h -BN monolayer [16,28], as well as the Cu $3d$ bands of the substrate between 2 and 4 eV binding energy. The second derivative has been applied to enhance sharpness and reduce the background intensity. Between the d -band maximum and the Fermi energy, another electronic state with negligible dispersion is visible just below 1 eV binding energy, which is not part of the Cu(111) or h -BN band structures. In Fig. 2 we compare this region in detail between the oxidized and unoxidized sample using He II α ARPES spectra.

The most prominent features are the Cu $3d$ bands with high intensity, and the He II β satellite of the h -BN π band. The binding energy of the π band decreases after the oxidation due to the increase in work function, as it is tied to the shifted vacuum level like the B $1s$ and N $1s$ states [28]. The unoxidized sample also exhibits the Shockley surface state (SS) of Cu(111) [30], whereas the latter disappears on the oxidized surface. The last feature is the shoulder above the d band in the oxidized sample, between 1 and 2 eV, that also appears in Fig. 1(c), but not on the unoxidized sample. We integrate the spectra between -0.7 and -1.2 \AA^{-1} for comparison without interference from the satellite and display the result with a Gaussian fit in Fig. 2(c). This feature must stem from the oxide layer, and density of states calculations have indeed predicted a hybridization of Cu $3d$ and O $2p$ orbitals at about 1 eV binding energy for chemisorbed oxygen on Cu(111) [31]. Thus, we assign this feature to the valence band maximum of the Cu₂O film at $1.28 \pm 0.01 \text{ eV}$.

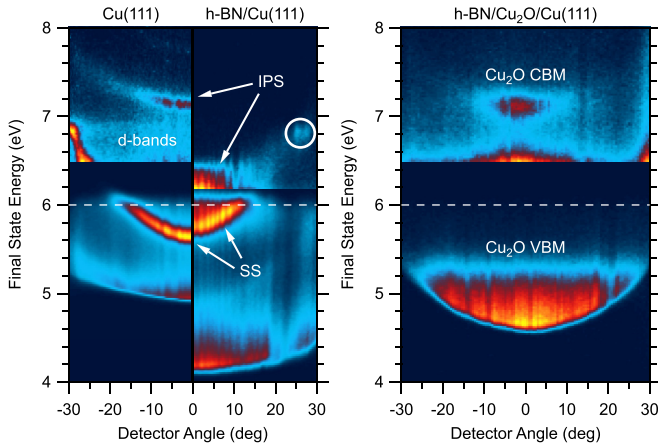


FIG. 3. Composite pump-only angle-resolved 2PPE and 3PPE spectra for bare Cu(111), *h*-BN/Cu(111), and *h*-BN/Cu₂O/Cu(111). The spectra are individually normalized and the relevant features are labeled. The dashed lines denote $E_F + 2h\nu$, and the white circle highlights the resonant transition between SS and IPS.

C. Unoccupied states

The unoccupied electronic states have been studied by static two-photon and three-photon photoemission (2PPE and 3PPE) using only the pump beam with low and high fluence, respectively. The 2PPE and 3PPE spectra for Cu(111), *h*-BN/Cu(111), and *h*-BN/Cu₂O/Cu(111) are combined in Fig. 3. The energy scale is the final state energy relative to the Fermi level, so the low energy cutoff of the spectra directly represents the work function. For Cu(111), it is measured at $\Phi = 4.9$ eV, with *h*-BN it drops to $\Phi = 4.1$ eV, and with the Cu₂O layer it rises again to $\Phi = 4.6$ eV. Electrons from the Fermi level appear at a final state energy of $2h\nu = 6.0$ eV, indicated by the dashed line. Energy values are given with no better than 0.1 eV accuracy because of surface inhomogeneities and space charge effects especially for the high fluences used in 3PPE. A work function map assessing the surface homogeneity after oxidation is included in Fig. S5 [27].

The occupied part of the Shockley surface state (SS) is well defined on Cu(111), and the unoccupied part is transiently populated by transitions from the *d* band and appears in the 3PPE spectrum [30]. Above the 3PPE *d*-band edge the first image potential state (IPS) [32] appears at 7.1 eV. Its binding energy relative to the vacuum level can be calculated as

$$E_{n=1} = \Phi - (E_{\text{final}} - h\nu) = 0.8 \text{ eV}.$$

The Shockley surface state binding energy is reduced by 0.1 eV on the *h*-BN covered surface, which is consistent with previous STM results [33]. The IPS is shifted down by 0.8–6.3 eV along with the vacuum level, which means that its binding energy remains the same. However, it cannot be accurately distinguished from the onset of the 2PPE spectrum. The Shockley state and the IPS have a different effective mass and intersect in a resonant transition at $E_{\text{final}} = 6.8$ eV, highlighted in the figure with a white circle.

On the oxidized surface the spectra look significantly different. The Shockley surface state is missing, and there is very little intensity above the Cu₂O valence band onset at 5.2 eV,

or $E - E_F = -0.8$ eV, because of the high surface sensitivity of 2PPE. Using sufficiently high pulse energy an unoccupied state appears in the 3PPE spectrum at $E_{\text{final}} = 7.1$ eV. The binding energy relative to the vacuum level would be only 0.5 eV if interpreted as an image potential state, and the spectral weight is concentrated at the $\bar{\Gamma}$ point in contrast to the clearly visible parabola in the other spectra. This leads us to the conclusion that it is not an IPS, but rather the conduction band minimum of the Cu₂O film at an energy of $E - E_F = 1.1 \pm 0.1$ eV.

D. Charge carrier dynamics

The charge carrier dynamics in this heterostructure have been measured with time-resolved 2PPE as described in the experimental methods. Figure 4 shows a time-resolved delay scan taken with 3 nJ pump pulse energy together with spectra at selected pump-probe delays and the detector image at $t = 50$ fs. The time-independent background has been subtracted. The short-lived conduction band occupation is visible at 0.95 ± 0.1 eV, and a much stronger state with long lifetime exists right above the Fermi level. This state is not discernible in the static 2PPE spectrum of Fig. 3 because it is not populated yet at $t = 0$. There is a diffuse background above it that extends over the whole energy range and has the same long relaxation time. The dispersion of the conduction band looks parabolic in the detector image, but the intense state close to E_F has no observable dispersion in the small accessible parallel momentum range. We assign this latter state to a localized oxygen vacancy defect state “DS1” that naturally occurs on oxygen-poor Cu₂O(111) surfaces close to the Fermi energy [34]. The long-lived states at higher energies can then be attributed to higher defect states “DS2,” following the terminology of a previous photoemission study on the $(\sqrt{3} \times \sqrt{3})R30^\circ$ reconstructed surface of bulk Cu₂O(111) that has demonstrated the efficient trapping of hot electrons in these two types of defect states [7]. In the extreme case of maximum defect density studied there, the conduction band is effectively quenched. In the present sample, we expect a smaller number of these defects. This means that we see a superposition of slowly decaying electrons in Cu₂O-like defect states which are populated by capturing the hot electrons from the metallic substrate, and of the hot electrons that pass the atomically thin oxide layer without being trapped.

We take a rate equation approach to model the hot electron dynamics. The pulse energy in our work equates to a fluence of $\sim 60 \mu\text{J}/\text{cm}^2$, which is in the low-excitation regime with negligible increase of the electronic temperature [35]. As the defect states are populated by capturing these hot electrons from the substrate, we describe their dynamics by another rate equation with the hot electron population as the source term. For simplicity, we will phenomenologically call the two components the “fast” and “slow” components. We obtain this system of differential equations:

$$\begin{aligned} \frac{d\rho_{\text{fast}}}{dt} &= a I(t - t_0) - \frac{\rho_{\text{fast}}}{\tau_{\text{fast}}}, \\ \frac{d\rho_{\text{slow}}}{dt} &= b \frac{\rho_{\text{fast}}}{\tau_{\text{fast}}} - \frac{\rho_{\text{slow}}}{\tau_{\text{slow}}}. \end{aligned}$$

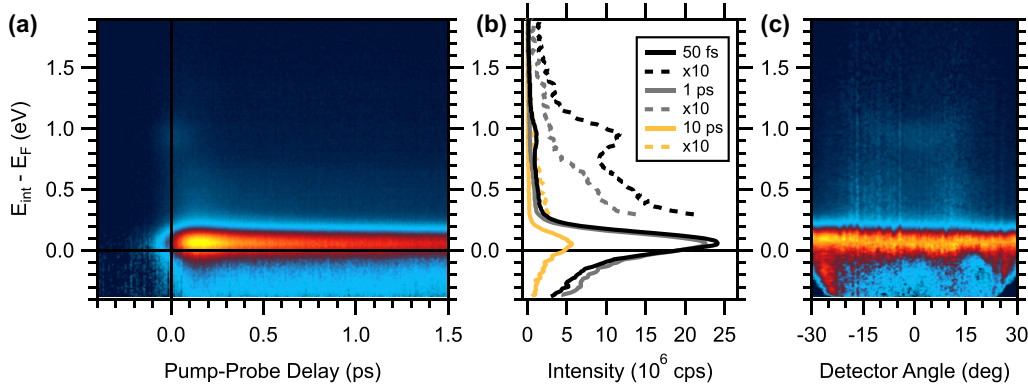


FIG. 4. (a) Time-resolved 2PPE scan after the first preparation, 3 nJ pump energy, linear color scale normalized to the maximum intensity. The spectra at negative delays were used for background subtraction. (b) Background-subtracted spectra at different delays. (c) Background-subtracted detector image at 50 fs delay, showing the dispersion of defect state and conduction band.

The first equation describes the change in hot electron population with the fast relaxation time τ_{fast} . The influence of the pump pulse is represented by the Gaussian pulse envelope $I(t - t_0)$, where $t - t_0$ is the delay between pump and probe pulse. The second equation is the change in defect state occupation, which is populated by capturing electrons from ρ_{fast} and decays with the slow relaxation time τ_{slow} . The intensities scale with the empirical parameters a and b .

We solve these equations numerically with a Runge-Kutta method to fit the transient intensities in 0.1-eV energy windows above the Fermi level as a function of pump-probe delay. The width of the Gaussian pulse envelope, corresponding to the laser pulse intensity cross correlation, is selected to produce the best fit agreement for all energies. This became necessary because a virtual state with no lifetime where the photoemission signal directly follows the laser pulse cross correlation is not available in this case. The relaxation time of the slow component is fixed in the same way because we do not observe a significant difference between the dynamics at low and high energies after the fast component has decayed, leaving only the maximum intensities of both components and the relaxation time of the fast component as free parameters. The transient intensities of the window at 1.0 eV containing the conduction band and the window at 0.1 eV containing the defect state DS1 are displayed as examples with their best fits in Fig. 5. The best overall fit agreement was found with a slow component relaxation time of 4 ps and a laser pulse intensity cross correlation with a full width at half maximum of 150 fs. We obtain a relaxation time of the fast component of 38 ± 20 fs at the conduction band energy, and 127 ± 20 fs at the defect state energy. Leaving t_0 as a free parameter leads to a better agreement with the data, in this case the source term shifts to later times for lower intermediate state energies. The shift is indicated by dashed vertical lines and amounts to 34 fs between the high and low energy trace. This indicates that secondary electrons from scattering events are dominating the source term for lower energy states. The presence of surface defects and disorder can provide these additional scattering channels, leading to electron cascades that are much stronger than on a pristine Cu(111) surface. We do not attempt to model the complex electron dynamics of the substrate in detail,

because secondary electron cascades and various additional effects were discussed in previous studies [35,36].

The fit results for the relaxation time of the fast component at each energy window from the Fermi level to the conduction band energy are compiled in Fig. 6. Besides the results for 3-nJ pulse energy, we also include results for 20-nJ pulse energy, which should be in the medium excitation regime at ~ 0.4 mJ/cm². This measurement was performed after the second preparation with a longer oxygen exposure. For comparison, we add our results for *h*-BN/Cu(111), obtained with a single rate equation, and literature results for Cu(111) from [37], obtained by fitting an exponential function to the decaying part of the delay trace after the intensity maximum. Note that this way, the effective relaxation times of the electron population are measured, instead of the bare electron-electron scattering lifetime predicted by Fermi liquid theory [38]. We see that the relaxation times agree quite well with those

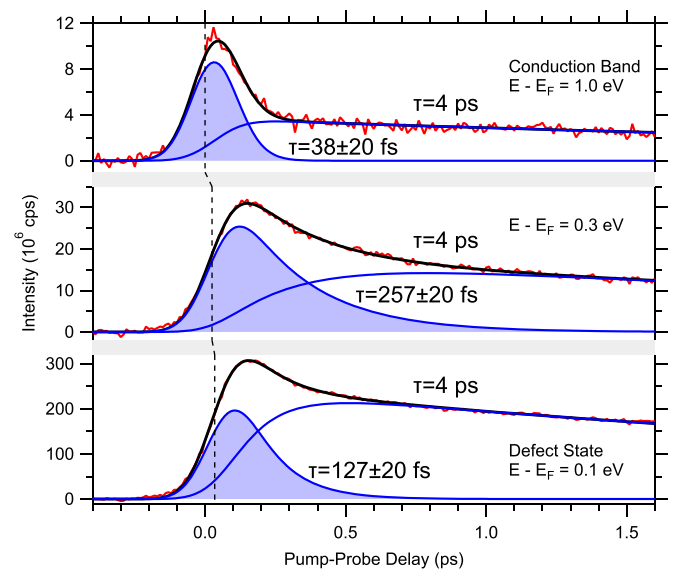


FIG. 5. Least-squares fits of electron dynamics at the conduction band energy, defect state energy and in between with the model described in the text.

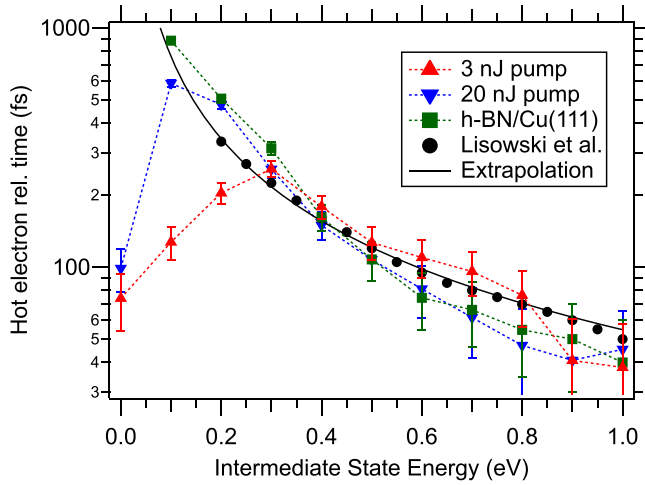


FIG. 6. Fit results for the relaxation time of hot electrons in the h -BN/Cu₂O/Cu(111) system excited with 3 and 20 nJ pump pulses. Fit results obtained with the same model on h -BN/Cu(111) and literature values for Cu(111) taken from [37] are included for comparison. The literature data are extrapolated to low energies.

observed in bulk copper, except at the lowest energies. For the energies close to the Fermi level, the relaxation times are reduced on the oxidized surface because of efficient electron capture in the defect state DS1 in contrast to the unoxidized h -BN/Cu(111) surface. The effective relaxation time for 20 nJ pump energy at low energies is longer than for 3 nJ pump energy, and we notice that the relative intensity of the defect state compared to the hot electrons is much smaller (see Fig. S7 [27]). This indicates that the longer oxygen exposure of the second preparation leads to a reduced defect density at the surface, and for a pump fluence high enough the defects are saturated. The relaxation time of the conduction band minimum at 1.0 eV, $\tau_{CBM} = 38 \pm 20$ fs, does not deviate from the hot electrons because it is also affected by fast electron capture, making it extremely short compared to bulk Cu₂O(111) where the initial relaxation time is $\tau_{CBM} = 2$ ps [7].

IV. DISCUSSION AND OUTLOOK

We have prepared an ordered surface oxide on Cu(111) protected by an h -BN layer through oxygen intercalation. XPS and ARPES spectra show that the h -BN layer stays intact. After oxidation a new state between E_F and the onset of the Cu d bands appears, which is reminiscent of the valence band of Cu₂O. The onset at $E - E_F \approx -0.8$ eV is lower than in p -type bulk Cu₂O where the Fermi level is found close to the valence band maximum [7], but agrees with DFT calculations for a surface oxide on Cu(111) [31]. The conduction band minimum was measured at 1.1 ± 0.1 eV in static 2PPE and 0.95 ± 0.1 eV in tr -2PPE, for an average value of 1.0 ± 0.2 eV. It is shifted the same way, as the conduction band minimum of p -type bulk Cu₂O has been measured at 1.6 eV [6,7]. Therefore, the band gap stays almost the same. We measure 1.8 ± 0.2 eV between the valence band onset at -0.8 eV and the conduction band at $+1.0$ eV, slightly smaller than the bulk value 2.1 eV [6,7] but reasonably close

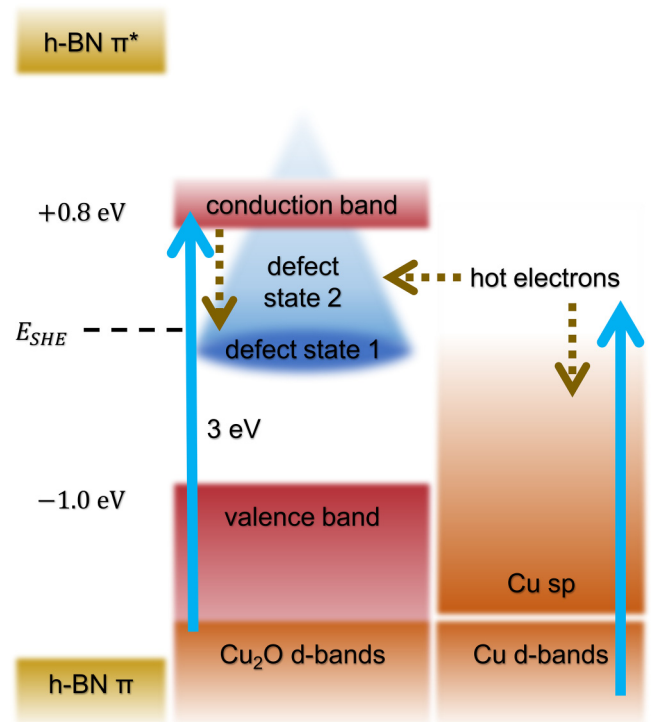


FIG. 7. Energy scheme of the heterostructure showing the different excitation and relaxation pathways.

despite the low thickness. STM studies have investigated the electronic density of states of thin cuprous oxide films on metal substrates and confirmed that the Cu₂O electronic states are shifted down due to the influence of the metal [39–41]. The different substrates and surface reconstructions exhibit slightly different electronic structures, but in general the lowest unoccupied states have been found approximately 0.8 eV above the Fermi level.

The proposed energy and excitation scheme for this heterostructure is sketched in Fig. 7. The wide band gap of the h -BN layer precludes any significant contribution to the electronic states close to E_F discussed here [18,42]. The light is predominantly absorbed in the copper substrate, creating a nonequilibrium distribution of hot electrons that we identified by their relaxation times. These electrons can subsequently populate the Cu₂O conduction band, the pronounced defect state DS1 at the Fermi level, and the broad defect state DS2 at higher energies. We seem to have a lower defect density than on the $(\sqrt{3} \times \sqrt{3})R30^\circ$ reconstructed Cu₂O(111) surface because there the conduction band is not visible at all and the defect states dominate the spectrum [6,7]. Only for the defect-free (1×1) reconstruction the conduction band could be measured with its relatively long lifetime of 10 ps [7]. The defect state DS1 has a high electron capture coefficient, which significantly reduces the relaxation time of low energy hot electrons. The hot electrons at higher energies show the usual relaxation dynamics of a Cu(111) surface. The relaxation time of the defect states varies with surface quality and excitation density. For the low fluence delay scan discussed in this paper the best fit was found with a relaxation time of 4 ps for both defect states. This is shorter than what has been measured on

bulk Cu₂O(111) [7]. We explain this with the high electron density of copper at the Fermi level, which increases the relaxation rate of the defect state through electron-electron scattering at the interface.

Finally, we will discuss the implications of our results for the viability of this heterostructure for photocatalysis. The challenges of Cu₂O photoelectrodes for solar energy conversion are discussed in [1], and the authors note that this material is an excellent candidate for use as a photocathode driving the hydrogen evolution reaction (HER). However, its chemical instability during operation in water, where the Cu₂O surface segregates into metallic Cu and insulating CuO grains, prevents its long-term use in an aqueous environment. Based on the corrosion resistance of *h*-BN/Cu(111) in water [13] we predict that the *h*-BN on our surface acts as a barrier for water molecules, which prevents the Cu₂O corrosion while allowing electrons to tunnel through for the HER. Moreover, the change in work function to $\Phi = 4.6$ eV shifts the energy scale with respect to the standard hydrogen electrode, which has an absolute potential of $E_{\text{SHE}} - E_{\text{vac}} = -4.44 \pm 0.02$ eV [43], so that $E_{\text{SHE}} - E_F \approx 0.2$ eV. The conduction band minimum lies 0.8 eV above the SHE, very similar to the conduction band position of bulk Cu₂O. This gives sufficient overpotential to efficiently drive the hydrogen evolution reaction. One concern is the trapping of hot electrons in oxygen vacancy defect states, but the longer oxygen exposure of our second prepara-

tion leads to an appreciable reduction of these defects, as seen in Fig. S7 [27]. Further refinement of the preparation parameters may improve the surface quality enough to offer similar performance to other cuprous oxide photocathodes with protective overlayers. Photoelectrochemical measurements of a device constructed with this material will be needed to quantify the efficiency and stability. Transferring the approach of *h*-BN deposition and oxygen intercalation to copper foil may turn this system into an economically viable photocathode with scalable production and easy handling of the flexible substrate.

All data used to produce the findings of this paper are publicly available on the Zenodo repository [44].

ACKNOWLEDGMENTS

The authors acknowledge funding from the Swiss National Science Foundation via NCCR MUST Project Grant Nos. 200020_172641 and 200020_200303. J.B. acknowledges financial support from the University of Zurich through UZH Candoc Grant No. FK-21-082. J.T.D. acknowledges financial support from the European Union's Horizon 2020 program via Grant No. FP-RESOMUS-MSCA 801459.

The authors declare no competing interests.

-
- [1] R. Wick and S. D. Tilley, Photovoltaic and photoelectrochemical solar energy conversion with Cu₂O, *J. Phys. Chem. C* **119**, 26243 (2015).
 - [2] A. Paracchino, V. Laporte, K. Sivula, M. Grätzel, and E. Thimsen, Highly active oxide photocathode for photoelectrochemical water reduction, *Nat. Mater.* **10**, 456 (2011).
 - [3] W. Niu, T. Moehl, W. Cui, R. Wick-Joliat, L. Zhu, and S. D. Tilley, Extended light harvesting with dual Cu₂O-based photocathodes for high efficiency water splitting, *Adv. Energy Mater.* **8**, 1702323 (2018).
 - [4] H. Li, Z. Su, S. Hu, and Y. Yan, Free-standing and flexible Cu/Cu₂O/CuO heterojunction net: A novel material as cost-effective and easily recycled visible-light photocatalyst, *Appl. Catal. B Environ.* **207**, 134 (2017).
 - [5] D. Chua, S. B. Kim, and R. Gordon, Enhancement of the open circuit voltage of Cu₂O/Ga₂O₃ heterojunction solar cells through the mitigation of interfacial recombination, *AIP Adv.* **9**, 055203 (2019).
 - [6] M. Borgwardt, S. T. Omelchenko, M. Favaro, P. Plate, C. Höhn, D. Abou-Ras, K. Schwarzburg, R. van de Krol, H. A. Atwater, N. S. Lewis, R. Eichberger, and D. Friedrich, Femtosecond time-resolved two-photon photoemission studies of ultrafast carrier relaxation in Cu₂O photoelectrodes, *Nat. Commun.* **10**, 2106 (2019).
 - [7] L. Grad, Z. Novotny, M. Hengsberger, and J. Osterwalder, Influence of surface defect density on the ultrafast hot carrier relaxation and transport in Cu₂O photoelectrodes, *Sci. Rep.* **10**, 10686 (2020).
 - [8] Y. Uchida, T. Iwaizako, S. Mizuno, M. Tsuji, and H. Ago, Epitaxial chemical vapour deposition growth of monolayer hexagonal boron nitride on a Cu(111)/sapphire substrate, *Phys. Chem. Chem. Phys.* **19**, 8230 (2017).
 - [9] T. A. Chen, C. P. Chuu, C. C. Tseng, C. K. Wen, H. S. P. Wong, S. Pan, R. Li, T. A. Chao, W. C. Chueh, Y. Zhang, Q. Fu, B. I. Yakobson, W. H. Chang, and L. J. Li, Wafer-scale single-crystal hexagonal boron nitride monolayers on Cu(111), *Nature (London)* **579**, 219 (2020).
 - [10] Q. Wu, J. H. Park, S. Park, S. J. Jung, H. Suh, N. Park, W. Wongwiriyan, S. Lee, Y. H. Lee, and Y. J. Song, Single crystalline film of hexagonal boron nitride atomic monolayer by controlling nucleation seeds and domains, *Sci. Rep.* **5**, 16159 (2015).
 - [11] L. Wang, X. Xu, L. Zhang, R. Qiao, M. Wu, Z. Wang, S. Zhang, J. Liang, Z. Zhang, Z. Zhang, W. Chen, X. Xie, J. Zong, Y. Shan, Y. Guo, M. Willinger, H. Wu, Q. Li, W. Wang, P. Gao *et al.*, Epitaxial growth of a 100-square-centimetre single-crystal hexagonal boron nitride monolayer on copper, *Nature (London)* **570**, 91 (2019).
 - [12] W. Auwärter, Hexagonal boron nitride monolayers on metal supports: Versatile templates for atoms, molecules and nanostructures, *Surf. Sci. Rep.* **74**, 1 (2019).
 - [13] F. Mahvash, S. Eissa, T. Bordjiba, A. C. Tavares, T. Szkopek, and M. Siaz, Corrosion resistance of monolayer hexagonal boron nitride on copper, *Sci. Rep.* **7**, 42139 (2017).
 - [14] D. Deng, K. S. Novoselov, Q. Fu, N. Zheng, Z. Tian, and X. Bao, Catalysis with two-dimensional materials and their heterostructures, *Nat. Nanotechnol.* **11**, 218 (2016).
 - [15] A. Lyalin, A. Nakayama, K. Uosaki, and T. Taketsugu, Functionalization of monolayer *h*-BN by a metal support for the oxygen reduction reaction, *J. Phys. Chem. C* **117**, 21359 (2013).

- [16] S. Roth, F. Matsui, T. Greber, and J. Osterwalder, Chemical vapor deposition and characterization of aligned and incommensurate graphene/hexagonal boron nitride heterostack on Cu(111), *Nano Lett.* **13**, 2668 (2013).
- [17] M. Wang, M. Kim, D. Odkhuu, N. Park, J. Lee, W.-J. Jang, S.-J. Kahng, R. S. Ruoff, Y. J. Song, and S. Lee, Catalytic transparency of hexagonal boron nitride on copper for chemical vapor deposition growth of large-area and high-quality graphene, *ACS Nano* **8**, 5478 (2014).
- [18] S. Lin, J. Huang, and X. Gao, A Cu(111) supported h-BN nanosheet: A potential low-cost and high-performance catalyst for CO oxidation, *Phys. Chem. Chem. Phys.* **17**, 22097 (2015).
- [19] J. T. Diulus, Z. Novotny, N. Dongfang, J. Beckord, Y. Al Hamdani, N. Comini, M. Muntwiler, M. Hengsberger, M. Iannuzzi, and J. Osterwalder, Towards 2D-confined catalysis on oxide surfaces (unpublished).
- [20] L. H. Li, T. Xing, Y. Chen, and R. Jones, Boron nitride nanosheets for metal protection, *Adv. Mater. Interfaces* **1**, 1300132 (2014).
- [21] M. Galbiati, A. C. Stoot, D. M. A. Mackenzie, P. Bøggild, and L. Camilli, Real-time oxide evolution of copper protected by graphene and boron nitride barriers, *Sci. Rep.* **7**, 39770 (2017).
- [22] M. Scardamaglia, V. Boix, G. D'Acunto, C. Struzzi, N. Reckinger, X. Chen, A. Shivayogimath, T. Booth, and J. Knudsen, Comparative study of copper oxidation protection with graphene and hexagonal boron nitride, *Carbon* **171**, 610 (2021).
- [23] Y. Yang, Q. Fu, M. Wei, H. Bluhm, and X. Bao, Stability of BN/metal interfaces in gaseous atmosphere, *Nano Res.* **8**, 227 (2015).
- [24] Q. Fu and X. Bao, Surface chemistry and catalysis confined under two-dimensional materials, *Chem. Soc. Rev.* **46**, 1842 (2017).
- [25] T. Greber, O. Raetz, T. J. Kreutz, P. Schwaller, W. Deichmann, E. Wetli, and J. Osterwalder, A photoelectron spectrometer for k-space mapping above the fermi level, *Rev. Sci. Instrum.* **68**, 4549 (1997).
- [26] M. Greif, L. Castiglioni, D. Becker-Koch, J. Osterwalder, and M. Hengsberger, Acquisition of photoelectron diffraction patterns with a two-dimensional wide-angle electron analyzer, *J. Electron Spectrosc. Relat. Phenom.* **197**, 30 (2014).
- [27] See Supplemental Material at <http://link.aps.org/supplemental/10.1103/PhysRevMaterials.7.045801> for XPS data and LEED images with brief discussion, work function maps, delay scans, and beam profiles, which includes Refs. [19,22,29,44–54].
- [28] A. Nagashima, N. Tejima, Y. Gamou, T. Kawai, and C. Oshima, Electronic Structure of Monolayer Hexagonal Boron Nitride Physisorbed on Metal Surfaces, *Phys. Rev. Lett.* **75**, 3918 (1995).
- [29] R. W. Judd, P. Hollins, and J. Pritchard, The interaction of oxygen with Cu(111): Adsorption, incorporation and reconstruction, *Surf. Sci.* **171**, 643 (1986).
- [30] A. A. Ünal, C. Tusche, S. Ouazi, S. Wedekind, C.-T. Chiang, A. Winkelmann, D. Sander, J. Henk, and J. Kirschner, Hybridization between the unoccupied Shockley surface state and bulk electronic states on Cu(111), *Phys. Rev. B* **84**, 073107 (2011).
- [31] A. Soon, M. Todorova, B. Delley, and C. Stampfl, Oxygen adsorption and stability of surface oxides on Cu(111): A first-principles investigation, *Phys. Rev. B* **73**, 165424 (2006).
- [32] E. V. Chulkov, V. M. Silkin, and P. M. Echenique, Image potential states on metal surfaces: Binding energies and wave functions, *Surf. Sci.* **437**, 330 (1999).
- [33] S. Joshi, D. Eciya, R. Koitz, M. Iannuzzi, A. P. Seitsonen, J. Hutter, H. Sachdev, S. Vijayaraghavan, F. Bischoff, K. Seufert, J. V. Barth, and W. Auwärter, Boron nitride on Cu(111): An electronically corrugated monolayer, *Nano Lett.* **12**, 5821 (2012).
- [34] C. Ricca, L. Grad, M. Hengsberger, J. Osterwalder, and U. Aschauer, Importance of surface oxygen vacancies for ultrafast hot carrier relaxation and transport in Cu₂O, *Phys. Rev. Res.* **3**, 043219 (2021).
- [35] E. Knoesel, A. Hotzel, T. Hertel, M. Wolf, and G. Ertl, Dynamics of photoexcited electrons in metals studied with time-resolved two-photon photoemission, *Surf. Sci.* **368**, 76 (1996).
- [36] E. Knoesel, A. Hotzel, and M. Wolf, Ultrafast dynamics of hot electrons and holes in copper: Excitation, energy relaxation, and transport effects, *Phys. Rev. B* **57**, 12812 (1998).
- [37] M. Lisowski, P. A. Loukakos, U. Bovensiepen, and M. Wolf, Femtosecond dynamics and transport of optically excited electrons in epitaxial Cu films on Si(111)-7 × 7, *Appl. Phys. A* **79**, 739 (2004).
- [38] M. Bauer and M. Aeschlimann, Dynamics of excited electrons in metals, thin films and nanostructures, *J. Electron Spectrosc. Relat. Phenomena* **124**, 225 (2002).
- [39] T. T. Ly, T. Lee, S. Kim, Y. J. Lee, G. Duvjir, K. Jang, K. Palotás, S. Y. Jeong, A. Soon, and J. Kim, Growing ultrathin Cu₂O films on highly crystalline Cu(111): A closer inspection from microscopy and theory, *J. Phys. Chem. C* **123**, 127116 (2019).
- [40] H. Sträter, H. Fedderwitz, B. Groß, and N. Nilius, Growth and surface properties of cuprous oxide films on Au(111), *J. Phys. Chem. C* **119**, 5975 (2015).
- [41] A. Gloystein and N. Nilius, Copper oxidation on Pt(111) – More than a surface oxide?, *J. Phys. Chem. C* **123**, 26939 (2019).
- [42] Q. Li, X. Zou, M. Liu, J. Sun, Y. Gao, Y. Qi, X. Zhou, B. I. Yakobson, Y. Zhang, and Z. Liu, Grain boundary structures and electronic properties of hexagonal boron nitride on Cu(111), *Nano Lett.* **15**, 5804 (2015).
- [43] S. Trasatti, The absolute electrode potential: An explanatory note (Recommendations 1986), *Pure Appl. Chem.* **58**, 955 (1986).
- [44] J. Beckord, J. T. Diulus, Z. Novotny, J. Osterwalder, and M. Hengsberger, Protected ultrathin cuprous oxide film for photocatalysis: Excitation and relaxation dynamics [Data set], (2023), <https://doi.org/10.5281/zenodo.7419322>.
- [45] C. Ma, J. Park, L. Liu, Y. S. Kim, M. Yoon, A. P. Baddorf, G. Gu, and A. P. Li, Interplay between intercalated oxygen superstructures and monolayer h-BN on Cu(100), *Phys. Rev. B* **94**, 064106 (2016).
- [46] S. Tanuma, C. J. Powell, and D. R. Penn, Calculations of electron inelastic mean free paths. V. Data for 14 organic compounds over the 50–2000 eV range, *Surf. Interface Anal.* **21**, 165 (1994).
- [47] R. Fasel, Adsorbed monolayers and submonolayers studied by angle-scanned photoemission, Ph.D. thesis, Universität Freiburg, 1996.

- [48] D. Tahir and S. Tougaard, Electronic and optical properties of Cu, CuO and Cu₂O studied by electron spectroscopy, *J. Phys.: Condens. Matter* **24**, 175002 (2012).
- [49] M. Schwarz, A. Riss, M. Garnica, J. Ducke, P. S. Deimel, D. A. Duncan, P. K. Thakur, T. L. Lee, A. P. Seitsonen, J. V. Barth, F. Allegretti, and W. Auwärter, Corrugation in the weakly interacting hexagonal-BN/Cu(111) system: Structure determination by combining noncontact atomic force microscopy and X-Ray standing waves, *ACS Nano* **11**, 9151 (2017).
- [50] C. Brülke, T. Heepenstrick, N. Humberg, I. Krieger, M. Sokolowski, S. Weiß, F. S. Tautz, and S. Soubatch, Long vertical distance bonding of the hexagonal boron nitride monolayer on the Cu(111) surface, *J. Phys. Chem. C* **121**, 23964 (2017).
- [51] F. Jensen, F. Besenbacher, E. Lægsgaard, and I. Stensgaard, Oxidation of Cu(111): Two new oxygen induced reconstructions, *Surf. Sci.* **259**, L774 (1991).
- [52] K. Moritani, M. Okada, Y. Teraoka, A. Yoshigoe, and T. Kasai, Reconstruction of Cu(111) induced by a hyperthermal oxygen molecular beam, *J. Phys. Chem. C* **112**, 8662 (2008).
- [53] N. A. Richter, C. E. Kim, C. Stampfl, and A. Soon, Revisiting the O/Cu(111) system - when metastable surface oxides could become an issue!, *Phys. Chem. Chem. Phys.* **16**, 26735 (2014).
- [54] J. Y. Zheng, T. K. Van, A. U. Pawar, C. W. Kim, and Y. S. Kang, One-step transformation of Cu to Cu₂O in alkaline solution, *RSC Adv.* **4**, 18616 (2014).